Infrared light management in high-efficiency silicon heterojunction and rear-passivated solar cells

Zachary C. Holman,[1,a)] Miha Filipič,[1,2] Antoine Descoeudres,[1] Stefaan De Wolf,[1] Franc Smole,[2] Marko Topič,[2] and Christophe Ballif[1]

[1]*École Polytechnique Fédérale de Lausanne (EPFL), Institute of Microengineering (IMT), Photovoltaics and Thin-Film Electronics Laboratory, Rue A.-L. Breguet 2, CH-2000 Neuchâtel, Switzerland*
[2]*University of Ljubljana, Faculty of Electrical Engineering, Tržaška 25, SI−1000 Ljubljana, Slovenia*

Silicon heterojunction solar cells have record-high open-circuit voltages but suffer from reduced short-circuit currents due in large part to parasitic absorption in the amorphous silicon, transparent conductive oxide (TCO), and metal layers. We previously identified and quantified visible and ultraviolet parasitic absorption in heterojunctions; here, we extend the analysis to infrared light in heterojunction solar cells with efficiencies exceeding 20%. An extensive experimental investigation of the TCO layers indicates that the rear layer serves as a crucial electrical contact between amorphous silicon and the metal reflector. If very transparent and at least 150 nm thick, the rear TCO layer also maximizes infrared response. An optical model that combines a ray-tracing algorithm and a thin-film simulator reveals why: parallel-polarized light arriving at the rear surface at oblique incidence excites surface plasmons in the metal reflector, and this parasitic absorption in the metal can exceed the absorption in the TCO layer itself. Thick TCO layers—or dielectric layers, in rear-passivated diffused-junction silicon solar cells—reduce the penetration of the evanescent waves to the metal, thereby increasing internal reflectance at the rear surface. With an optimized rear TCO layer, the front TCO dominates the infrared losses in heterojunction solar cells. As its thickness and carrier density are constrained by anti-reflection and lateral conduction requirements, the front TCO can be improved only by increasing its electron mobility. Cell results attest to the power of TCO optimization: With a high-mobility front TCO and a 150-nm-thick, highly transparent rear ITO layer, we recently reported a 4-cm^2 silicon heterojunction solar cell with an active-area short-circuit current density of nearly 39 mA/cm^2 and a certified efficiency of over 22%. © 2013 American Institute of Physics. [http://dx.doi.org/10.1063/1.4772975]

I. INTRODUCTION

Silicon heterojunction solar cells have been reported with minority carrier effective lifetimes at one-sun injection levels that approach the Auger and radiative recombination limit of the silicon wafer base.[1,2] Significant improvements in open-circuit voltage (V_{oc}) are thus expected only if the wafer is thinned.[3,4] Consequently, increasing short-circuit current density (J_{sc}) or fill factor (FF) is a more promising route to further improving device efficiency. This contribution focuses on J_{sc}. External quantum efficiency (EQE) and total reflectance (R) spectra provide a complete accounting of the fate of light incident on a solar cell in short-circuit conditions, allowing quick identification of J_{sc} losses. EQE interpretation is simplified for high-carrier-lifetime heterojunction solar cells, as the collection efficiency of carriers generated in the wafer is approximately unity and thus current losses are associated solely with light not absorbed in the wafer.

To motivate the present investigation, consider the EQE and total absorbance (1-R) spectra in Fig. 1(b) of heterojunction cells (Fig. 1(a)) co-deposited in our laboratory on wafers 100 and 250 μm thick. All light is reflected (area above dashed 1-R curves), absorbed in the wafer and converted to current (area below solid EQE curves), or absorbed parasitically in, e.g., the amorphous silicon (a-Si:H) and transparent conductive oxide (TCO) layers (area between EQE and 1-R). In identifying and quantifying losses, it is convenient to divide the spectra into two wavelength regions.

For short wavelengths—those well below 1000 nm, for which $1/\alpha \ll d$, where α is the absorption coefficient of the wafer and d is the wafer thickness—little light is reflected thanks to a pyramidally textured front surface and a TCO anti-reflection coating. Between 600 and 1000 nm, almost all absorbed light is successfully converted to current, so that the EQE and 1-R curves nearly touch (unity internal quantum efficiency). For shorter wavelengths, the curves separate. Eliminating this parasitic absorption would result in a proportional gain in EQE; the EQE curves would move upward to meet the 1-R curves, which would remain fixed. We previously showed that for 20.8%-efficient heterojunction solar cells, J_{sc} is reduced by 2.1 mA/cm^2 because of parasitic absorption at wavelengths below 600 nm.[5] This J_{sc} loss—the largest in our cells—is predominantly due to bandgap absorption in the front intrinsic and doped a-Si:H layers, with only a minor contribution (0.3 mA/cm^2) from bandgap absorption in the TCO. Thinner a-Si:H layers, or more transparent substitute materials, would mitigate the parasitic absorption.

At long wavelengths—those well above 1000 nm, for which $1/\alpha \gg d$—total reflectance increases as the wafer
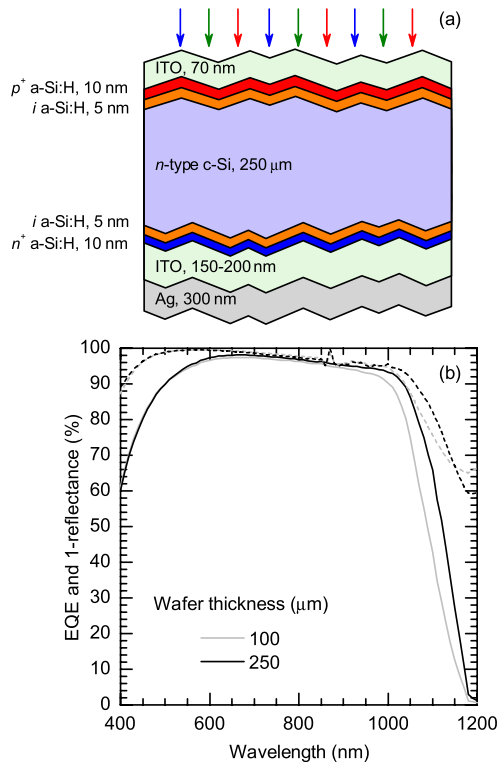
a)zachary.holman@epfl.ch.

113, 013107-1

FIG. 1. (a) Schematic of the silicon heterojunction solar cells fabricated in this work, including the default layer thicknesses used unless otherwise stated. (b) External quantum efficiency (solid) and 1-reflectance (dashed) of silicon heterojunction solar cells co-deposited on wafers 100 and 250 μm thick.

becomes transparent and secondary escape reflection is added to the primary front-surface reflection. (Escape reflection refers to light that enters the cell, undergoes one or more internal reflections, and subsequently exits through the front.) Parasitic absorption also increases, and roughly 50% of 1150 nm light is absorbed but generates no current. Were this absorption to be eliminated, the extra light would be redistributed between both EQE and R, so that the EQE and 1-R curves would move towards each other.[6,7] For the 250-μm-thick cell in Fig. 1(b), 0.7 mA/cm^2 is lost to infrared (IR) parasitic absorption, while 1.2 mA/cm^2 is lost for the 100-μm-thick cell. Reducing IR parasitic absorption thus represents another important opportunity for J_{sc} improvement, one that becomes more significant for thinner wafers because less light is absorbed in the active layer between each internal reflection at the lossy surfaces. Light trapping—the minimization of reflectance at near-bandgap wavelengths by increasing the optical pathlength with novel textures—has the potential to dramatically increase IR EQE as well, if the Yablonovitch limit can be exceeded.[8] However, no light-trapping scheme has of yet surpassed this limit for a broad range of wavelengths, and the random pyramid texture employed both in our and in industrial silicon cells already approaches the limit: Only 0.4 mA/cm^2 less current is collected in the 250-μm-thick cell in Fig. 1(b) than in an equivalent cell with Lambertian scattering, and 0.6 mA/cm^2 less is collected in the 100-μm-thick cell.

All solar cells have poor conversion efficiency for wavelengths near the active-layer bandgap, motivating many pre-

vious light-management studies for non-heterojunction silicon devices.[6,7,9–16] However, IR light management in silicon heterojunction solar cells is neither like that in diffused-junction crystalline silicon solar cells nor like that in thin-film silicon cells. Heterojunction cells and monocrystalline diffused-junction cells share the same random pyramid texture at the silicon surfaces, so that the angular distribution of light paths—and thus the probability of absorption in the wafer or escape out the front—is similar in both devices in the absence of parasitic absorption.[9] However, there is parasitic absorption in both devices, and it is different. Heterojunction solar cells require a TCO layer at the front to transport charge laterally, and a TCO layer is commonly employed at the rear as well. Free carriers in these layers absorb IR light, including the 1000–1200 nm photons that one would like to be absorbed in the wafer instead. In rear-passivated silicon solar cells, non-absorbing dielectric films of, e.g., silicon oxide, silicon nitride, or aluminum oxide are found in place of the TCO, eliminating this source of parasitic absorption. Thus, in terms of IR light propagation, silicon heterojunction solar cells are like rear-passivated cells with absorbing dielectric passivation layers. Thin-film microcrystalline silicon solar cells, by contrast, have a similar TCO/crystalline silicon/TCO/rear reflector structure to heterojunction cells and therefore face similar parasitic absorption. However, thin-film cells are grown on substrates with textures that differ significantly from micrometer-sized pyramids, so that the distribution of light paths in each device type is unique. Consequently, an independent investigation of IR light management in silicon heterojunction solar cells is required.

This paper analyzes IR parasitic absorption in silicon heterojunction cells, focusing on the front and rear TCO layers and the silver rear reflector. Only indium tin oxide (ITO) is considered, though the trends we elucidate are general and apply to most materials systems. Sputtered ITO was chosen because it is the most common TCO in heterojunction solar cells, and its thickness and carrier density can be easily tuned, making it a model system. In simulating IR light propagation, we develop a general framework, and consider the specific case of transparent TCO layers with an imperfect metal reflector. This structure is optically identical to silicon solar cells with dielectric rear passivation, allowing us to extend the heterojunction analysis to absorption losses in the metal reflector of diffused-junction cells with local rear contacts. Experimental results in which the front, then rear, ITO layer is independently varied are presented first. Simulations of single internal reflections at the surfaces of a solar cell follow for variable ITO thickness and doping, and the cumulative effect of many internal reflections (resulting in the cell's total reflectance) is calculated. Finally, we compare IR parasitic absorption in the front and rear ITO layers to determine which most limits J_{sc}.

II. EXPERIMENTAL

Silicon heterojunction solar cells were fabricated using processes described in detail elsewhere.[1,17] Briefly, n-type float-zone wafers ((100), 4 Ω cm, 250 μm thick unless otherwise stated) were textured on both sides with random

pyramids in an alkaline solution. a-Si:H layers were deposited via plasma-enhanced chemical vapor deposition (PECVD) after chemical cleaning. An intrinsic/p-type a-Si:H stack was deposited on the front (sunward) side to form the hole collector (i.e., emitter), and an intrinsic/n-type a-Si:H stack was deposited on the rear side to form the electron collector (i.e., back surface field). Importantly, depositions were performed in a large-area industrial reactor with high spatial uniformity so that, within a given experiment, all wafers were co-deposited with identical a-Si:H layers. Quasi-steady-state photoconductance measurements revealed minority carrier effective lifetimes of a few milliseconds and implied V_{oc}s of over 720 mV.

ITO was sputtered from an In_2O_3/SnO_2 target onto both sides of the wafers, and layer thicknesses were adjusted by varying the deposition time. The rear ITO layers covered the entire wafer surfaces, whereas the front ITO films were deposited through a shadow mask to define three 4-cm^2 solar cells per wafer. Oxygen gas was introduced into the chamber during sputtering, and the ITO free-carrier density was tuned from 10^{19} to 10^{21} cm^{-3} by varying the oxygen partial pressure.[18] Unless purposefully varied, front ITO layers were nominally 70 nm thick with carrier mobilities and densities of 30 cm^2/Vs and 3×10^{20} cm^{-3}, respectively. Rear ITO layers were nominally 150–200 nm thick with mobilities and densities of 25 cm^2/Vs and 3×10^{19} cm^{-3}. In some optical experiments, a non-absorbing silicon nitride (SiN$_x$) layer deposited by PECVD was substituted for an ITO layer.[19] A silver reflector roughly 300 nm thick was sputtered over the entire rear surface, and a silver front grid was screen-printed on the front of each cell. A finger spacing of 2.2 mm was used for all cells; this value was calculated to be optimal, given a TCO sheet resistance of 75 Ω/sq and fingers 100 μm wide and 30 μm tall. As during PECVD, sputtered ITO and silver layers were co-deposited for cells within each experimental series (save the layer purposefully varied), so that only screen-printing was performed on a per-wafer basis. A glass witness sample was included during each ITO and SiN$_x$ deposition for layer characterization. Finally, wafers (and witness substrates) were annealed at 200 °C to cure the printed silver paste.

The thicknesses of ITO and SiN$_x$ layers were measured on the planar glass witness samples with a profilometer. The thicknesses on the pyramidally textured wafer surfaces—those reported throughout this paper—were calculated by dividing by 1.7. This surface area ratio was confirmed by comparing the wavelengths of reflectance minima for co-deposited films on planar and textured wafers, taking into account the wavelength-dependent refractive index. Carrier mobility and density were determined from Hall effect measurements in the Van der Pauw geometry on the witness samples. For select ITO and SiN$_x$ layers, spectroscopic ellipsometry was employed to determine the complex refractive indices (n and k). Ellipsometric spectra were recorded at two angles (50 and 70°) on layers deposited on single-side polished silicon wafers with a 300-nm-thick thermal silicon oxide. This substrate was chosen because it minimizes rear side specular reflection and provides interference enhancement, which increases the information gathered when using

multiple angles of incidence.[20] In addition, transmittance spectra were measured at normal incidence for ITO or SiN$_x$ layers on glass that were co-deposited with the ellipsometry samples. The transmittance and two ellipsometry spectra were fit simultaneously with a bound model, giving a unique solution for n and k. The ITO layers were modeled with a Tauc-Lorentz-Drude dispersion relation, and the SiN$_x$ layers with a Tauc-Lorentz relation. The Tauc-Lorentz and Drude relations simulate bandgap and free-carrier absorption, respectively.

EQE and *R* were measured on the active area of (non-metallized) cells. *EQE* measurements were performed with a setup that employs a lock-in technique to measure the current generated under monochromatic illumination and compare it with that of a calibrated photodiode. A dual-beam spectrophotometer equipped with an integrating sphere collected all reflected light during reflectance measurements. Aperture-area current-voltage (I-V) measurements were performed on complete (metallized) cells under Air Mass 1.5 global illumination. Each cell-performance value reported is an average from three cells on the same wafer, and error bars indicate the standard deviation of the mean. Note that this measure of error does not incorporate run-to-run variation.

The reflectance, transmittance, and absorbance of planar three-layer optical stacks were calculated from the generalized Fresnel equations using the one-dimensional transfer-matrix method.[21,22] Calculations were performed separately for light polarized parallel and perpendicular to the plane of propagation, and the results were averaged to simulate unpolarized sunlight in a solar cell. The simulated structures were silicon/ITO/air and silicon/ITO/silver, representing the front and rear of heterojunction solar cells, respectively. The ITO was substituted with SiN$_x$ for select simulations to isolate absorption in the silver; this configuration also corresponds to rear-passivated diffused-junction solar cells. The first and last layers were treated as semi-infinite and the thickness of the middle layer was varied. The simulations used as inputs the complex refractive indices determined from ellipsometry of our ITO and SiN$_x$ layers, and published refractive indices of monocrystalline silicon and silver.[23,24] All simulations were performed at the sub-silicon-bandgap wavelength of 1200 nm and the angle of incidence was varied from 0 to 90°.

To reproduce the measured reflectance of complete solar cells, the above matrix formalism (wave optics) was coupled to a three-dimensional incoherent ray tracing algorithm (geometric optics) using the CROWM optical simulator.[25] Light propagation in the double-side textured silicon wafer was determined by ray tracing, while the matrix method calculated the reflectance and transmittance at the front and rear surfaces using the angles passed to it from the ray tracer. Two surface textures were investigated: a regular array of 5-μm-tall pyramids with a characteristic angle of 54.7°, and random pyramids measured with atomic force microscopy (AFM) on a solar cell. A wafer thickness of 250 μm was assumed. For each simulation, 600 normally incident rays were placed at random locations on the front surface and traced.

III. RESULTS AND DISCUSSION

A. Front TCO: Cell results

The front TCO layer in silicon heterojunction solar cells plays both optical and electrical roles. It serves as an anti-reflection coating, like the front dielectric layer in diffused-junction solar cells. With a refractive index of $n_{TCO} \approx 2$ at visible wavelengths, the layer must be 65–80 nm thick on random pyramid surfaces to maximize J_{sc}. The TCO also replaces the emitter of diffused-junction solar cells as the lateral transport medium for charges to the metallic grid electrode, since millimeter-scale conduction through the a-Si:H emitter is not possible. The power lost to Joule heating in the front TCO is proportional to its sheet resistance, which is given by $R_{sh} = (eN\mu t)^{-1}$, with e the electrical charge, and N, μ, and t the TCO free-carrier density, mobility, and thickness, respectively. As thickness is fixed by the anti-reflection requirement and mobility is limited by the chosen TCO material, carrier density is the only tunable parameter to adjust the front TCO's contribution to series resistance. Figure 2 shows the dependence of heterojunction cell performance on the front ITO carrier density. As anticipated, FF falls rapidly with decreasing carrier density; when the x-axis is changed to the front ITO sheet resistance, the FF dependence is linear.

J_{sc} also depends strongly on carrier density, and trends in the opposite direction of FF. An optimum is found when the marginal change in J_{sc} with carrier density is equal to that of FF. We reported previously that for sputtered ITO with $\mu = 30$ cm²/Vs (as in Fig. 2) this condition is reached for our cells when $N = 3 \times 10^{20}$ cm⁻³.[5] This value was used for all experiments unless otherwise stated.

In Fig. 3, EQE and 1-R spectra are plotted for four of the cells in Fig. 2. The 1 mA/cm² loss in J_{sc} over the range of carrier densities investigated is attributable to IR parasitic absorption in the front ITO. This is consistent with the Drude model, according to which the absorption coefficient for free-carrier absorption scales with carrier density and inversely with mobility.[26] Notice that, because the front TCO is
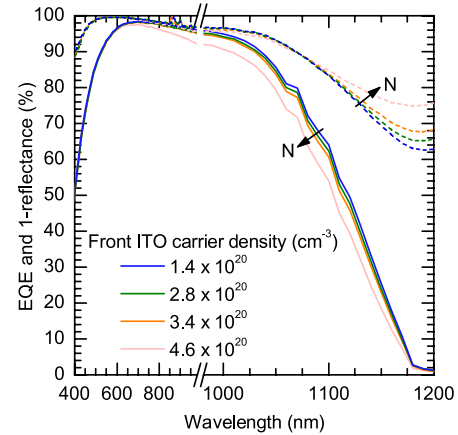
FIG. 3. External quantum efficiency (solid) and 1-reflectance (dashed) of co-deposited solar cells with varying front ITO doping. These spectra were measured on the cells in Fig. 2. The bumps in the EQE spectra near 1100 nm are caused by a change in calibration diodes.

the first layer encountered by incident light, high-N TCOs erode J_{sc} both at wavelengths greater than 1000 nm—for which light interacts with the front TCO multiple times as it bounces in the wafer—and at 600–1000 nm wavelengths—for which light passes through the front TCO only once. In addition, the TCO refractive index deviates from the geometric mean of the air and silicon indices as carrier density becomes large (see Fig. 8), reducing the effectiveness of the TCO layer as a broadband anti-reflection coating. This effect becomes even more severe in modules because encapsulants have refractive indices of approximately 1.5. Both absorption below 1000 nm and increased primary front-surface reflectance (just visible near 1025 nm) are apparent in Fig. 3 for the cell with $N = 4.6 \times 10^{20}$ cm⁻³. The only way to circumvent the FF-J_{sc} trade-off is to develop high-mobility front TCO layers so that carrier density may be reduced while maintaining satisfactory sheet resistance.

B. Rear TCO: Cell results

There is little discussion in the literature of the rear TCO in silicon heterojunction solar cells.[27–29] In bifacial cells, the rear TCO requirements are like those of the front TCO, though higher sheet resistances may be tolerated if the wafer is sufficiently conductive. In cells with full rear metallization (like those presented here), however, both the anti-reflection and lateral transport constraints are relieved. In this case, it is unclear how the rear TCO should be designed, if such a layer should be included at all. In particular, thickness and carrier density are seemingly unconstrained, and their effects on cell performance unknown.

The I-V characteristics of cells with rear ITO layers 0–300 nm thick are summarized in Fig. 4. For our sputtered ITO, carrier density and mobility tend to decrease with thickness for constant deposition conditions. Consequently, the oxygen partial pressure during sputtering was adjusted to keep μ/N approximately constant and $N < 10^{20}$ cm⁻³, for which free-carrier absorption in the rear ITO is small compared to in the front ITO (see Fig. 15). Because of the challenge in making identical layers with varying thickness, the
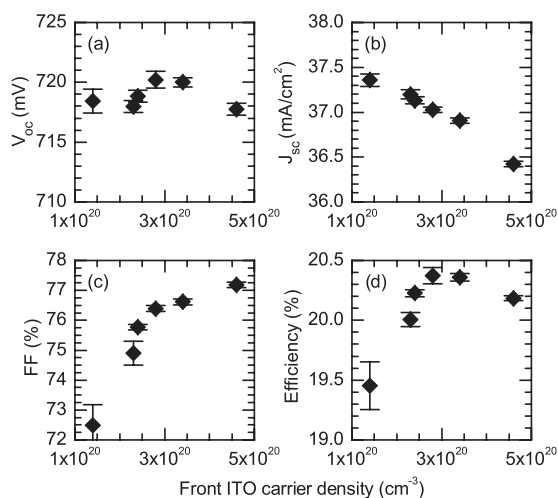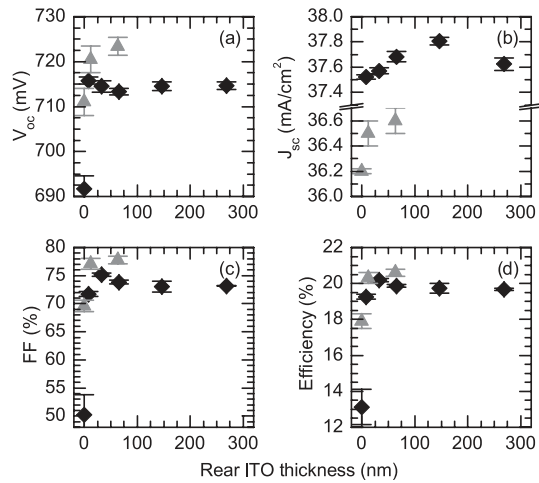

FIG. 2. Output characteristics of co-deposited 4-cm² solar cells with varying front ITO doping. The mobility and thickness varied by less than 5% across the data set. Each data point represents the average value of three cells.

FIG. 4. Output characteristics of 4-cm² solar cells with varying rear ITO thickness. Two sample series are shown (grey triangles: standard layers; black diamonds: low-*N* front ITO), and all layers within each series were co-deposited, save the rear ITO layer. As ITO carrier density decreases with thickness for the same deposition conditions, the oxygen flow during sputtering was adjusted to keep $N < 10^{20}\,\mathrm{cm}^{-3}$. Each data point represents the average value of three cells.

experiment was performed twice. The grey triangles in Fig. 4 correspond to cells deposited with our standard recipes, whereas the black diamonds correspond to cells with a very transparent front ITO layer (hence the large J_{sc} and small *FF* values). *FF* decreases by 8% (absolute) in one case and over 20% in the other when the rear ITO layer is omitted, and is otherwise independent of the layer thickness. The I-V characteristics of cells without rear ITO layers are S-shaped, indicating a reversed diode, and V_{oc} decreases in addition to *FF*. A rear ITO layer thus acts as an important electrical contact layer when a silver rear reflector is used. Note, though, that this role is specific to the materials system: ITO (or any other TCO) may not form low-resistance Ohmic contacts to all metals and doped a-Si:H layers,[30–33] and there may be doped a-Si:H/metal combinations that form Ohmic junctions without a TCO interlayer. For example, Bivour *et al.* recently reached an impressive *FF* of 81.5% for a rear-emitter silicon heterojunction cell with no TCO between the highly doped *p*-type emitter and the silver reflector.[29]

Figure 4 also reveals that the rear TCO appears to have a second, optical role: for low-*N* rear ITO layers, J_{sc} increases with thickness, then saturates. If high-*N* ($>1 \times 10^{20}\,\mathrm{cm}^{-3}$) rear ITO layers are instead used, J_{sc} decreases with thickness (not shown). *EQE* and 1-*R* spectra for the cells in Fig. 4 are presented in Fig. 5. Apparently, there is less IR parasitic absorption in cells with thicker rear ITO layers, resulting in greater *EQE* and J_{sc}. This is not intuitive: for constant μ/N, thicker ITO layers absorb more light (neglecting interference effects). The explanation involves evanescent waves that penetrate through the TCO and are absorbed in the silver reflector. The effect will be explored in detail in Sec. III C. The optimum rear ITO thickness is approximately 150 nm. This value was used for all experiments unless otherwise stated.

The effects of the rear ITO carrier density on cell performance are shown in Figs. 6 and 7. First, *FF* shows no dependence on the rear TCO doping for $N < 2 \times 10^{20}\,\mathrm{cm}^{-3}$.
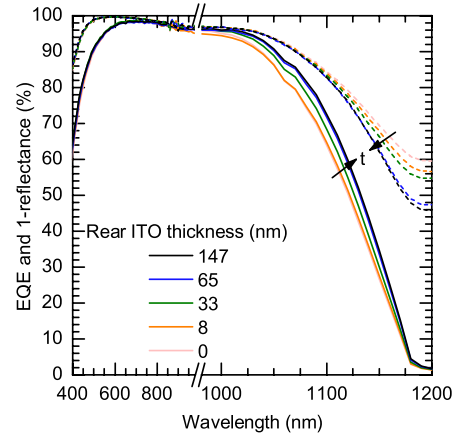

FIG. 5. External quantum efficiency (solid) and 1-reflectance (dashed) of co-deposited solar cells with varying rear ITO thickness. These spectra were measured on the cells represented by black diamonds in Fig. 4.

(The low *FF* obtained for the highest-*N* cell is surprising, but is perhaps attributable to a change in work function as the ITO becomes degenerately doped.[30,34]) This is because lateral conduction is not needed in the rear TCO when full rear metallization is used, and thus the sole contribution to series resistance is contact resistance. For the ITO and sputtered silver rear reflector stack used here, contact resistance is relatively insensitive to carrier density but this cannot be assumed for other materials systems.

Second, J_{sc} falls with increasing doping. As with the front ITO layer (Fig. 3), the *EQE* and 1-*R* curves confirm that the source of the loss is free-carrier absorption (Fig. 7). There are, however, two notable differences between changing carrier density in the front and rear ITO layers. First, *EQE* is more sensitive to the value of *N* in the rear ITO layer. We will show later that this is primarily due to its greater thickness. Second, even the highest-*N* rear ITO does not decrease *EQE* at short wavelengths (unlike for the front ITO; cf. Fig. 3 at 600–1000 nm) because these wavelengths are fully absorbed in the wafer and never "see" the back of the
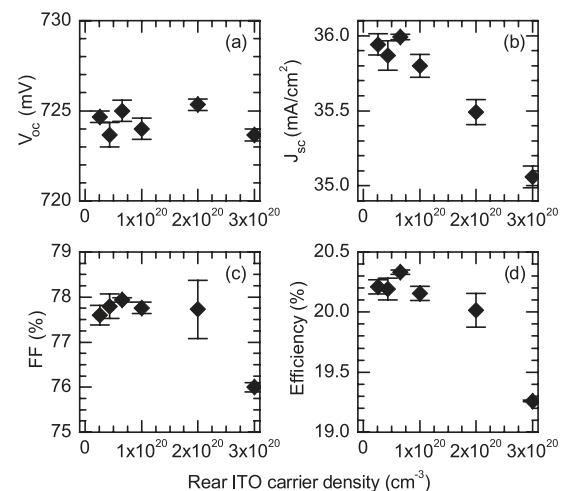

FIG. 6. Output characteristics of co-deposited 4-cm² solar cells with varying rear ITO doping. Mobility and thickness varied by less than 20% and 5%, respectively, across the data set. Each data point represents the average value of three cells.
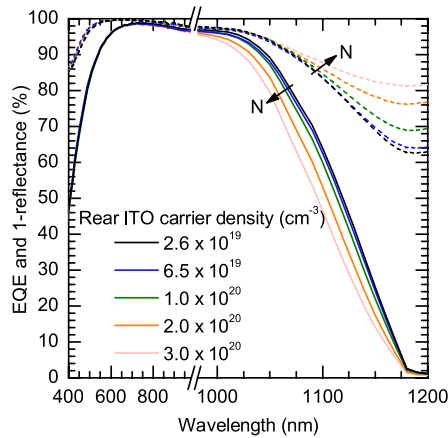
FIG. 7. External quantum efficiency (solid) and 1-reflectance (dashed) of co-deposited solar cells with varying rear ITO doping. These spectra were measured on the cells in Fig. 6.

cell. As only J_{sc} depends strongly on carrier density, provided good electrical contact is achieved, the best rear TCO is the most IR-transparent (largest μ/N). This is an atypical requirement; most TCO applications have a maximum acceptable sheet resistance and thus TCOs with $N < 10^{20}\,cm^{-3}$ are rarely of interest. Superior performance may even be possible with layers that are not TCOs, like the moderately conductive filamentary silicon oxide films introduced by Cuony *et al.*[35]

C. Physics of light-TCO and light-metal interactions

We turn now to the physics of parasitic absorption inside a silicon heterojunction solar cell by calculating the Fresnel transmission and reflection coefficients for a beam of light incident on the (locally planar) front TCO/air or rear TCO/ metal interfaces from silicon. The analysis also explains and quantifies absorption in the metal reflector of rear-passivated diffused-junction silicon solar cells, as these cells correspond to the special case of non-absorbing TCO layers. All simulations used 1200 nm light because it is just below the silicon bandgap and therefore not absorbed in the active layer. Consequently, any absorption at 1200 nm reduces R exclusively and not EQE, which is zero. 1-R at 1200 nm is thus a metric of parasitic absorption. Indeed, absorption at any sub-bandgap wavelength is parasitic. However, we chose 1200 nm so that we can extend our findings to 1000–1200 nm—for which parasitic absorption *does* reduce EQE—without encountering large changes in the complex refractive indices. All results are for unpolarized light unless otherwise stated.

The ITO complex refractive indices determined from ellipsometry and used in simulations are given in Fig. 8. These five sets of n and k values reflect the whole range of ITO layers explored. For the SiN$_x$ layers used to imitate non-absorbing ITO, $n = 2.05$–1.90 and $k = 0$ over the relevant wavelength range.

1. Qualitative description of internal reflection

Before advancing to the simulation results, we seek an intuitive understanding of internal reflection and parasitic absorption by considering Fig. 9, in which all possible paths

for light in the wafer arriving at the front and rear surfaces are depicted. (For a discussion of the primary reflection of light incident from air, see Refs. 36 and 37.) For illustration, ITO refractive indices of 1.6 and 2.0 were assumed for the front and rear ITO layers, respectively, as these are the values in Fig. 8 for our best front and rear layers. Other values simply change the critical angles and pathlengths according to Snell's law. We emphasize that the following qualitative analysis is insightful but overly simplistic, especially for ITO layers less than 200 nm thick and angles of incidence above the silicon/ITO critical angle ($\theta_{c,\,Si/ITO}$).[38]

Light incident on the front surface from inside the silicon active layer will follow one of three paths, labeled a_f, b_f, and c_f in Fig. 9, depending on the angle of incidence relative to the pyramid surface (θ). (We are fortunate to be able to make such a categorization; a similar treatment is not possible for thin-film silicon cells since the texture size is on the order of the wavelength of light.) Light arriving outside the $\theta_{c,\,Si/ITO} = 27°$ transmission cone is represented by path a_f. Were the ITO to be replaced by a non-absorbing dielectric, such as SiN$_x$, light following path a_f would undergo total internal reflection with an evanescent wave decaying exponentially into the SiN$_x$ layer. With lossy ITO, however, the light undergoes attenuated total reflection, and the field in the ITO layer is no longer purely evanescent; some energy is transported across the silicon/ITO interface and is absorbed. (Nevertheless, for simplicity we will use "evanescent" to describe this attenuated, evanescent-like wave.) The physics here is the same as in the popular attenuated total reflection Fourier transform infrared (ATR-FTIR) spectroscopy technique. A thorough qualitative and quantitative analysis of attenuated total reflection can be found in Harrick *et al.*[38–40] Parasitic absorption in thick ITO layers depends on n_{ITO}/n_{si}, θ, α, and the penetration depth of the evanescent wave, d_p, which itself depends on the first two parameters. The closer n_{ITO}/n_{si} is to unity, the greater the interaction of the evanescent wave with the film. For the refractive indices in our example and a wavelength of 1200 nm, the penetration depth varies from 67 nm at $\theta = 89°$ to 340 nm at $\theta = 28°$, and
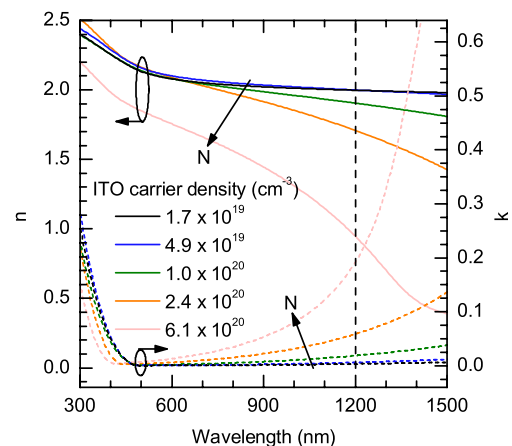

FIG. 8. Real (solid) and imaginary (dashed) parts of the complex refractive index of ITO layers with varying doping. The optical constants were determined via ellipsometry. All simulations were performed using the values along the vertical dashed line at 1200 nm.
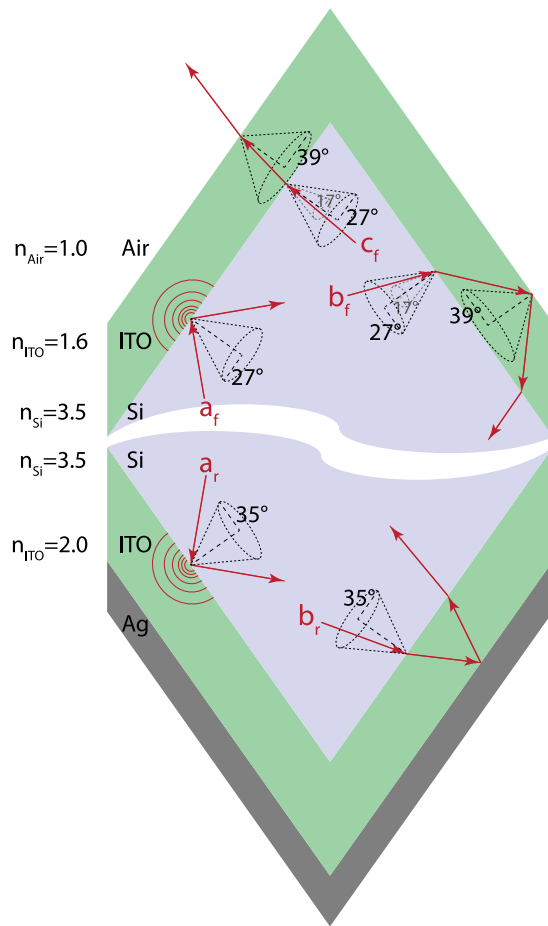
FIG. 9. Schematic of internal reflection paths at the front and rear of a silicon heterojunction solar cell. a_f, b_f, and c_f have angles of incidence of 45°, 20°, and 5°, respectively. a_r and b_r have angles of incidence of 45° and 15°, respectively. Refractive indices of 1.6 and 2.0 have been assumed for the front and rear ITO layers, respectively, as these values are typical for our best films at 1200 nm. The transmission cones are drawn at each interface, and the critical angles are given. The 17° gray cones at the front silicon/ITO interface correspond to $\theta_{c, Si/air}$, the maximum escape angle for light in the wafer.

finally becomes infinite at the $\theta_{c, Si/ITO} = 27°$ transition to propagating waves. As a point of reference, for $\theta = 45°$, the absorbance of the evanescent wave is approximately the same as that of a propagating wave traversing an optical pathlength of 100 nm. For larger angles of incidence, this "effective thickness" of absorption falls rapidly, whereas it grows as θ approaches $\theta_{c, Si/ITO}$. Thus, in terms of absorption, light following path a_f is equivalent to light transmitted normally through a film tens to hundreds of nanometers thick. For very thin films (for which $t \ll d_p$), light propagation is determined exclusively by the refractive indices of the materials on either side of the layer (i.e., $\theta_{c, Si/ITO}$ no longer matters),[38] and the above guidelines break down. As the penetration depth is angle-dependent, many of the films we consider in our simulations are "thick" for large angles of incidence, but "thin" for θ near $\theta_{c, Si/ITO}$.

Path b_f corresponds to light arriving inside the $\theta_{c, Si/ITO} = 27°$ transmission cone but outside the $\theta_{c, ITO/air} = 39°$ cone, i.e., $27° < \theta < \theta_{c, Si/air} = 17°$. Light is totally internally reflected at the ITO/air interface, and the attenuation in the

ITO layer is given by the exponential decay law, taking into account the extended pathlength as light traverses the ITO layer twice. For layers with thicknesses on the order of the wavelength, interference must also be considered. Interference will not alter the transmitted wave, which is always zero because of total internal reflection, but it will enhance or diminish the absorbed and reflected intensities. Finally, path c_f is taken by light that is within both transmission cones and thus exits the cell. The attenuation in the ITO layer again follows the exponential decay law, though the pathlength is less than half that for path b_f because the light only traverses the layer once, and at a smaller angle. For path c_f, interference alters reflection, absorption, and transmission.

At the rear surface, there are only two possible internal reflection paths. For thick ITO films, paths a_r and a_f are identical because the evanescent waves do not penetrate deep enough to see the ITO/silver and ITO/air interfaces. For thinner layers, the evanescent wave may couple to the silver rear reflector and the reflectance loss is the sum of the absorbance in the ITO and silver layers. The magnitude of the coupling is difficult to predict prior to simulation, but we note that a silver layer may interact with propagating and evanescent modes very differently, and thus exhibit high reflectance at near-normal angles while absorbing at oblique angles. The physics associated with path a_r is the same as that in metal-overlayer ATR-FTIR, a little-known but interesting technique for enhancing absorption in monolayer films.[41,42] Light within the $\theta_{c, Si/ITO} = 35°$ transmission cone travels path b_r and traverses the ITO layer twice. This path is similar to b_f, but the attenuation is modified by any loss that may exist in the silver reflector. Interference augments or decreases the losses in both layers.

2. Simulation of single internal reflections

Simulations of single internal reflections at the front and rear surfaces of heterojunction solar cells appear in Figs. 10–12, and much of the behavior can be understood in the context of the above qualitative discussion. The internal reflectance (into silicon), ITO absorbance, and transmittance (into air) at the front of a heterojunction solar cell are plotted in Fig. 10 as function of the angle of incidence. The ITO carrier density was varied, as was done experimentally (Figs. 2 and 3), and a SiN$_x$ layer was simulated for comparison. The layer thickness was set to 75 nm in accordance with the anti-reflection requirement. a-Si:H layers were excluded because $n_{a\text{-}Si:H} \approx n_{Si}$ at 1200 nm and measurements indicate that their contribution to IR parasitic absorption is negligible. Consider first the ITO layer with $N = 2.4 \times 10^{20} \, \text{cm}^{-3}$, which is similar to the best front ITO layer experimentally identified. The angle ranges corresponding to paths a_f, b_f, and c_f in Fig. 9 are given at the top of Fig. 10 for this ITO. The ITO absorbance increases gradually with angle for path c_f, consistent with the increasing pathlength. The reflectance and transmittance are determined by the Fresnel equations and are nearly the same as for the SiN$_x$ layer, since the ITO absorbance is small. At $\theta_{c, Si/air} = 17°$, the transmittance drops to zero as the ITO/air interface becomes totally internally reflecting, and the absorbance doubles as the pathlength through ITO doubles. The absorbance continues to increase with angle for
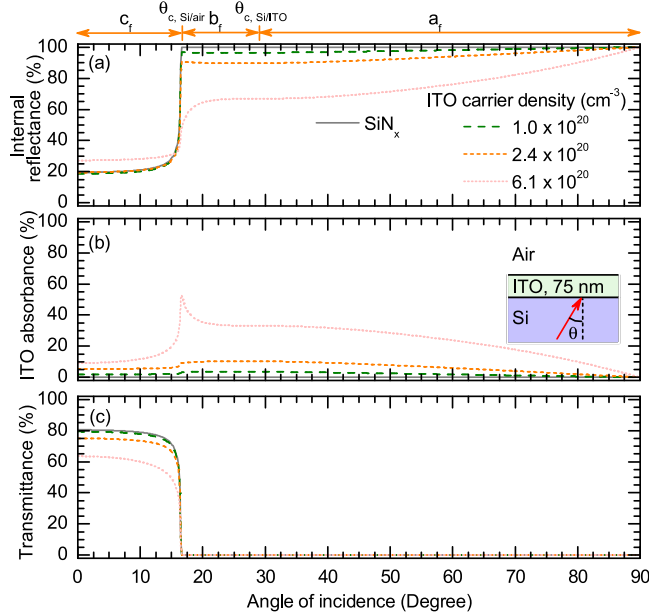
FIG. 10. Simulated internal reflectance, ITO absorbance, and transmittance of 1200 nm light at the front silicon/ITO/air interface as a function of angle of incidence. The ITO thickness was fixed at 75 nm and the carrier density was varied. The two most transparent ITO layers are not plotted as they fall between the dashed green and solid grey curves. Data are also plotted for a substitute SiN_x layer, as is used in most diffused-junction cells. The angle ranges corresponding to paths a_f, b_f, and c_f in Fig. 9, as well as the two critical angles, are given at the top of the figure for the ITO layer with $N = 2.4 \times 10^{20} cm^{-3}$.
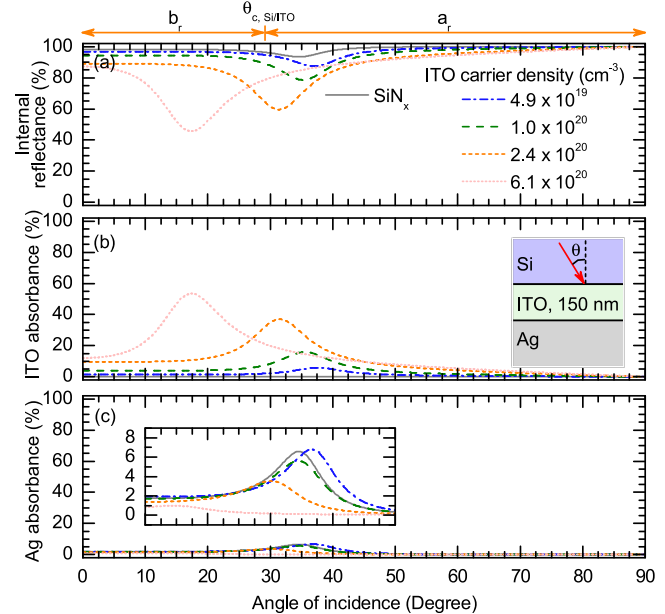
FIG. 11. Simulated internal reflectance, ITO absorbance, and silver absorbance of 1200 nm light at the rear silicon/ITO/silver interface as a function of angle of incidence. The ITO thickness was fixed at 150 nm and the carrier density was varied. The most-transparent ITO layer is not plotted as it nearly overlaps the dash-dotted blue curve. Data are also plotted for a substitute SiN_x layer. The inset in (c) shows the same data as in (c) and uses the same x-axis, but the y-axis scale has been adjusted. The angle ranges corresponding to paths a_r and b_r in Fig. 9, as well as the critical angle, are given at the top of the figure for the ITO layer with $N = 2.4 \times 10^{20} cm^{-3}$.

path b_f, then decreases as the wave becomes evanescent after the transition to path a_f. The greatest parasitic absorption occurs near $\theta_{c, Si/ITO}$, for which the pathlength (for the propagating modes at $\theta < \theta_{c, Si/ITO}$) or the penetration depth (for the evanescent modes at $\theta > \theta_{c, Si/ITO}$) is greatest.

As ITO doping increases, the absorbance grows for all angles of incidence, explaining the IR parasitic absorption observed experimentally in Fig. 3. Note that $N = 6.1 \times 10^{20} cm^{-3}$ is a coincidentally odd case, since $n_{ITO} \approx 1$ for this layer (see Fig. 8) and thus $\theta_{c, Si/ITO} = \theta_{c, Si/air}$. Consequently, path b_f does not exist and the ITO absorbance spikes at the sole critical angle. For $N < 10^{20} cm^{-3}$, parasitic absorption in the front ITO becomes relatively unimportant (consistent with Fig. 3), with less than 4% of light lost per reflection at all angles. If we were able to design the angular distribution function of light arriving at the front surface, we would aim for oblique angles. In this case, diffused-junction solar cells with non-absorbing dielectric coatings such as SiN_x would exhibit perfect light trapping at the front surface, and parasitic absorption in the front TCO layers of heterojunction cells would be minimized.

Internal reflection at the rear is somewhat different. Figure 11 is the same as Fig. 10 but now light is incident on the rear ITO/silver reflector stack, and absorbance in the silver layer is plotted in place of transmittance. The rear ITO layer thickness was fixed at 150 nm, as per our best experimental results. Paths a_r and b_r from Fig. 9 are again indicated for the ITO layer with $N = 2.4 \times 10^{20} cm^{-3}$ to illustrate the relationship between the simulated results and qualitative analysis, although for the rear ITO layer this doping density is too high to be optimal. As at the front of the cell, ITO absorb-

ance increases for both propagating (path b_r) and evanescent (path a_r) waves as θ approaches $\theta_{c, Si/ITO}$. Absorption in ITO is not the only loss, however; there is also absorption in the silver layer that peaks near $\theta_{c, Si/ITO}$. (If the silver is replaced with aluminum or copper, the shape of the absorbance curve remains the same but the values increase.) This parasitic absorption in the silver is present—and is, in fact, largest—when the rear ITO layer is replaced by a SiN_x layer, as in diffused-junction solar cells with dielectric rear passivation. As carrier density increases, ITO absorbance grows while silver absorbance diminishes. Their sum always increases with ITO carrier density, although not for each angle since the absorption peak shifts as the ITO refractive index changes. Consequently, for nearly any angular distribution function, rear reflectance is reduced with ITO doping, eroding IR *EQE*, as was observed experimentally in Fig. 7. For our best, lowest-N ITO layers, we calculate that 88% of light is internally reflected per reflection at $\theta_{c, Si/ITO}$, and more than 96% for angles not within 8° of $\theta_{c, Si/ITO}$. For the nonabsorbing SiN_x layer, these values increase to 93% and 97%, respectively.

The curves in Fig. 11 apply only for an optimized rear ITO thickness of 150 nm, and Fig. 5 revealed that IR *EQE* and *R* are sensitive to this thickness in finished cells. Figure 12 maps reflectance and absorbance for a single internal reflection at the rear of a heterojunction solar cell as a function of the ITO thickness. Areas of high reflectance and absorbance appear white; low values are black. To read these maps, first study the grey dashed line in the fifth row, which slices the reflectance and absorbance maps at a rear ITO thickness of
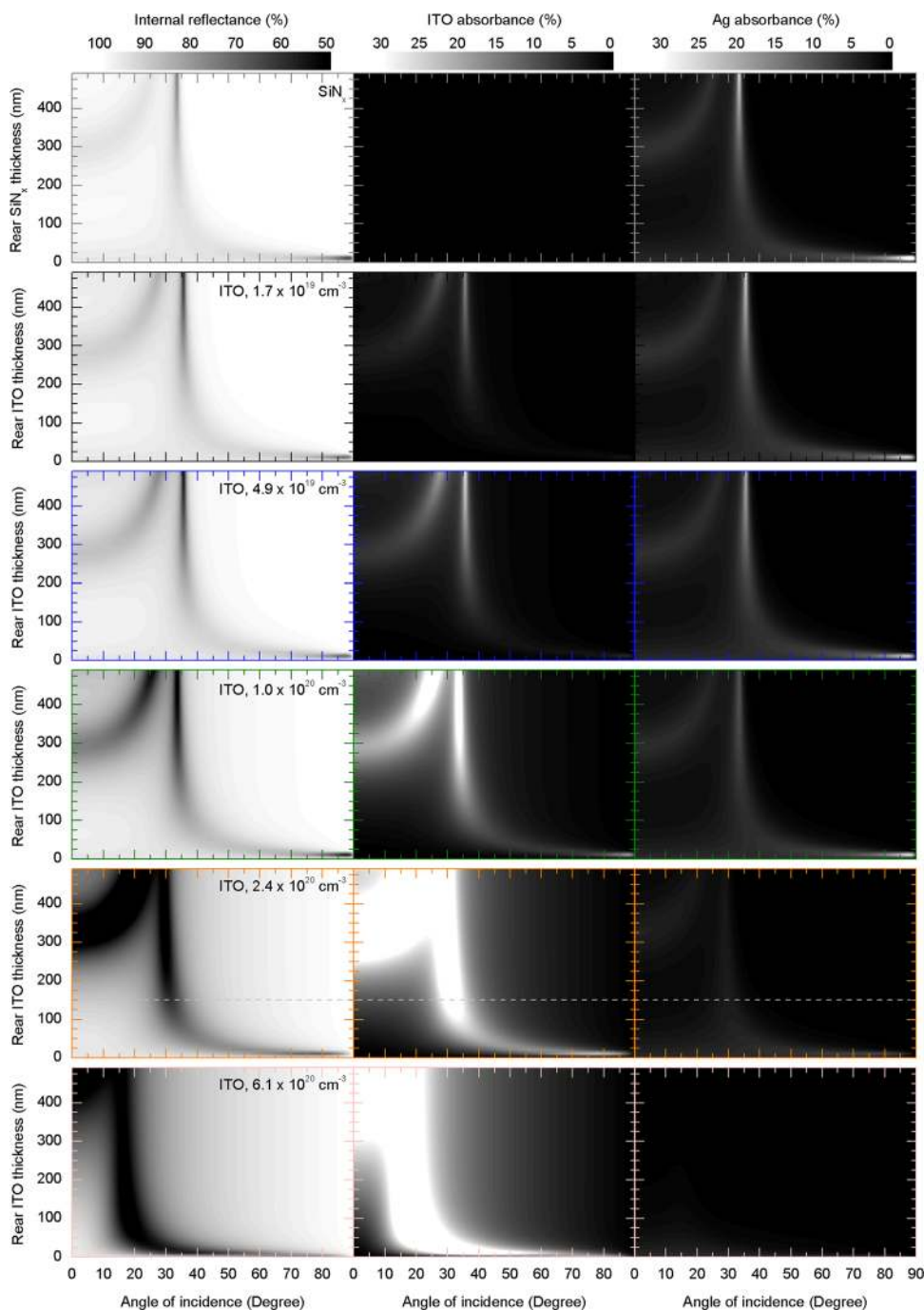
FIG. 12. Simulated maps of internal reflectance (left column), ITO absorbance (middle column), and silver absorbance (right column) of 1200 nm light at the rear silicon/ITO/silver interface as a function of angle of incidence and ITO thickness. Each row of maps corresponds to a different carrier density; data is also plotted for a substitute SiN$_x$ layer. Note that the right two columns have the same contrast scale, but the left column has a unique scale. This was necessary to avoid losing valuable information. The dashed grey line in the fifth row at a rear ITO thickness of 150 nm is intended to aid interpretation; the data along the line appear in Fig. 11 in a more traditional representation.

150 nm. The information along this line is identical to that in Fig. 11 for the same ITO layer ($N = 2.4 \times 10^{20}$ cm^{-3}), but the y-scale has been replaced with a contrast scale.

For a non-absorbing SiN$_x$ substitute layer like those in rear-passivated diffused-junction solar cells (top row), absorption in the silver reflector is the only source of reflection loss. For layers less than 20 nm thick, there is very strong absorption—more than 25% absorbance per internal reflection—but only at high angles. Consistent with the findings of Ishino and Ishida,[41] our simulations indicate that this absorption occurs only for waves polarized parallel to the plane of propagation (transverse magnetic). The evanescent field of parallel-polarized light may excite surface plasmon polaritons, resulting in strong electric fields; indeed, the simulated structure is simply the Otto configuration with the air gap replaced by SiN$_x$.[43] Plasmonic losses have been reported in thin-film silicon solar cells but the excitation mechanism is often different.[44,45] In thin-film cells with random textures, rough surfaces scatter light into localized plasmonic modes; in the Otto configuration, parallel-polarized evanescent modes excite surface plasmons at flat interfaces. This high-angle coupling explains our observations that silver is an excellent reflector in solar cells on double-side polished wafers but is very lossy on wafers with the front side textured and the rear side polished. In the first case, all light hits the rear reflector normally and there are few internal reflections, whereas the angular distribution in the latter case evolves to include high angles that result in absorption in the silver, even though the rear surface is mirror polished.

As the SiN_x layer thickens, the silver absorption peak becomes narrower and weaker (before resurging and finally disappearing; not shown), and shifts to smaller angles, consistent with Otto's findings.[43] For thicknesses greater than approximately 200 nm, the evanescent field "sees" the silver only for angles near $\theta_{c,\,Si/SiNx}$, where d_p—and thus the field strength—remains large. Consequently, the absorption peak settles near $\theta_{c,\,Si/SiNx}$ and there is no absorption at higher angles; the SiN_x film has become optically thick to most evanescent waves and thus behaves in the manner discussed for path a_r in Fig. 9. Others have pointed out the utility of a dielectric buffer layer in suppressing plasmon excitation at the rear of thin-film silicon solar cells.[45,46] These studies found somewhat different behavior, however, because the nanostructured substrates investigated induce localized surface plasmons even for normally incident light. For propagating modes ($\theta \leq \theta_{c,\,Si/SiNx}$), the silver layer continues to absorb, even for thick SiN_x films. Besides the peak at $\theta_{c,\,Si/SiNx}$, another "branch" is introduced in the silver absorbance map at a thickness of 300 nm, and it moves towards $\theta_{c,\,Si/SiNx}$ for thicker films. This is due to interference: For a wavelength of 1200 nm and $n_{SiNx} = 1.9$, normally incident light is constructively coupled to the silver layer for SiN_x thicknesses that are multiples of approximately 300 nm. The role of the SiN_x thickness is thus twofold: it controls both the evanescent (i.e., plasmonic) and interference coupling to the silver layer. The optimum thickness minimizes their sum.

Because the electric field strength is large at the silver surface only if it is also large within the SiN_x or ITO film, the ITO absorbance maps have the same shape as the silver maps. There are two exceptions. First, thick ITO layers absorb at angles much greater than $\theta_{c,\,Si/ITO}$ because the evanescent field continues to probe the first d_p nanometers of the ITO layer even when the silver layer is out of reach. This is most easily seen for the highest-N ITO layers since they have the largest absorption coefficient. Second, ITO layers less than 100 nm thick do not absorb appreciable light at small angles of incidence, but the silver layer behind them does. The internal reflectance maps for high-transparency rear ITO layers—those with $N < 10^{20}\,cm^{-3}$ that were determined to be best for cells in Fig. 6—are nearly the same as for SiN_x. For example, for the ITO layer with $N = 1.7 \times 10^{19}\,cm^{-3}$ in Fig. 12, reflectance is still overwhelmingly determined by absorption in the silver layer, with a non-negligible contribution from the ITO layer only for films greater than 200 nm thick. As carrier density increases beyond $10^{20}\,cm^{-3}$, however, absorption in the ITO layer becomes the dominant reflection loss. Consequently, we anticipate two optimization regimes: For mildly doped ITO, the optimal layer thickness minimizes absorption in the silver layer; for highly doped ITO, the best thickness minimizes absorption in the ITO. For all ITO and SiN_x films, one would like light to arrive at the rear reflector at only acute angles (for films less than 50 nm thick) or oblique angles (for thicker films).

3. Simulation and measurement of total reflectance

To return to solar cells we must calculate the *average* loss per internal reflection at the front and rear surfaces. This

may be achieved by integrating the angle-dependent reflectance curves in Figs. 10 and 12 (we leave thickness variable at the rear) over an assumed angular distribution function, which will undoubtedly *not* contain only low or high angles. The total reflectance of a solar cell at 1200 nm (the reflectance that one measures, not internal reflectance) may then be deduced by summing the transmittance out of the front of the cell over many internal reflections and adding this escape reflectance to the primary front-surface reflectance. A Lambertian angular distribution of light is likely achieved after several internal reflections, but this approximation is crude for the first few bounces and is better suited to the analysis of thin-film devices with nanoscale textures.[9,47] We chose instead to employ a ray tracer to track rays inside the cell, obviating the need to assume an angular distribution function at all. For each internal reflection, the tracer knows the angle of incidence and can thus adopt the appropriate results from Fig. 10 or 12 directly. A distribution function is generated by the tracer by noting these angles over many internal reflections, and it depends on the assumed surface texture. We imported a height map of random pyramids acquired by AFM (Fig. 13(a)) and used this texture for both the front and rear of our simulated cell. For comparison, ray tracing was also performed with a regular pyramid texture on the front and rear (Fig. 13(b)).
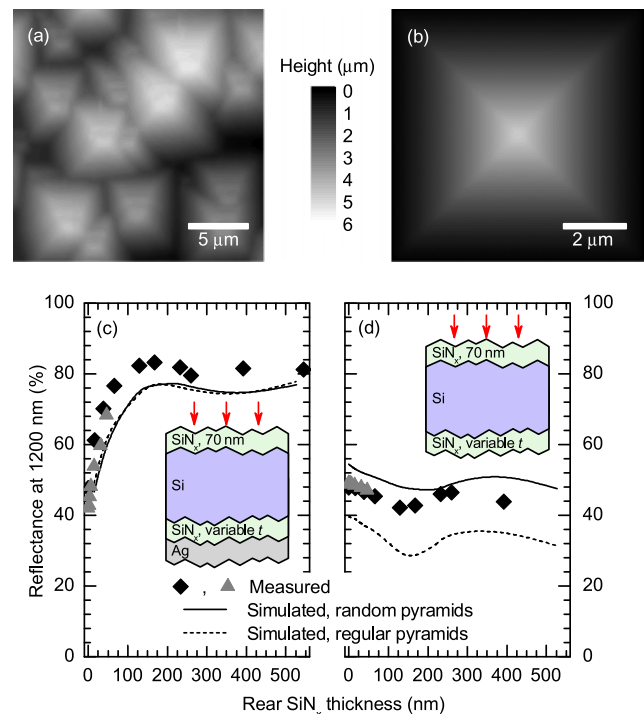

FIG. 13. (a) Random and (b) regular pyramid textures used at the front and rear surfaces of the simulated optical structures. The random texture was obtained by measuring a height map of a textured wafer with AFM. The image in (a) was mirrored across both the x- and y-axes before simulation so that the resulting texture was continuous. This is required by ray tracers, and also explains why the single pyramid in (b) simulates pyramids tiled regularly. Measured and simulated total reflectance of 1200 nm light incident on textured wafers with front and rear SiN_x layers, (c) with and (d) without a silver layer at the rear. The two sets of experimental data correspond to wafers textured with nominally the same process, but one year apart. To form the simulated curves, the reflectance was calculated for ten rear SiN_x thicknesses, and splines were fit to the results.

Optical simulations and experimental results appear in Fig. 13. First, absorption in the silver was isolated by depositing SiN_x layers at the front (70 nm) and rear (variable thickness) of wafers without a-Si:H layers, as in rear-passivated diffused-junction cells. The total reflectances of the same structures were simulated. With a silver reflector at the rear, the measured reflectance increases dramatically as the SiN_x layer is thickened to 150 nm (Fig. 13(c)). For thicker layers, the reflectance remains high and oscillates with small amplitude. The simulated reflectance follows the same trends but with slightly smaller values; further simulations revealed that the absolute value of the reflectance (but not the curve shape) is sensitive to the assumed texture (although, coincidently, the two textures presented here give similar results). Texture sensitivity is observed experimentally as well: The two experimental data sets were measured on identical wafers textured one year apart with nominally the same process. From Fig. 12, we anticipate that the shape of the reflectance for rear SiN_x thicknesses less than 300 nm is determined by absorption of evanescent waves, whereas the shape for greater thicknesses is dictated by interference of propagating waves. This is confirmed in Fig. 13(d), which presents the reflectance of the same samples prior to silver deposition. Without the silver reflector, only interference alters the reflectance. Its effect is minor because light with $\theta \leq \theta_{c, Si/SiNx}$ still arrives with a wide range of angles, smearing out the interference extrema. (Note that the sensitivity of the simulated reflectance to the assumed texture is evident here.) Thus, the principal reason a 150-nm-thick SiN_x film produces the best reflectance—and a 150-nm-thick transparent ITO layer produces the best *EQE*—is because it removes the silver layer sufficiently far from the wafer surface to reduce coupling of high-angle, parallel-polarized light. Nonetheless, for an optimized SiN_x layer, 15% of incident light is still absorbed parasitically in the silver rear layer. This loss may be reduced with a low-*n* dielectric (e.g., silicon dioxide or magnesium fluoride) that narrows the transmission cone.[48] Local rear contacts would then be required, but such a reflector could be employed in either heterojunction or diffused-junction cells.

With ITO instead of SiN_x at the rear of the simulated structure, the total reflectance decreases with increasing carrier density for any given layer thickness (Fig. 14). Nevertheless, for ITO layers with $N < 10^{20} \, cm^{-3}$, maximum reflectance is still achieved with a layer approximately 150 nm thick. Recall that this was observed experimentally in Fig. 5; the black diamonds in Fig. 14 are taken from the measured reflectance curves in that figure. For highly doped ITO, however, total reflectance decreases near-monotonically with increasing layer thickness because free-carrier absorption in the ITO exceeds plasmonic absorption in the silver, even for thin layers. This has implications for cells with detached rear reflectors and highly doped rear TCO layers that transport charge laterally to a rear metallization grid. J_{sc} in these cells, which include Sanyo's HIT modules with white back sheets, will decrease with rear ITO layer thickness, though the ITO sheet resistance will improve and may increase *FF*.
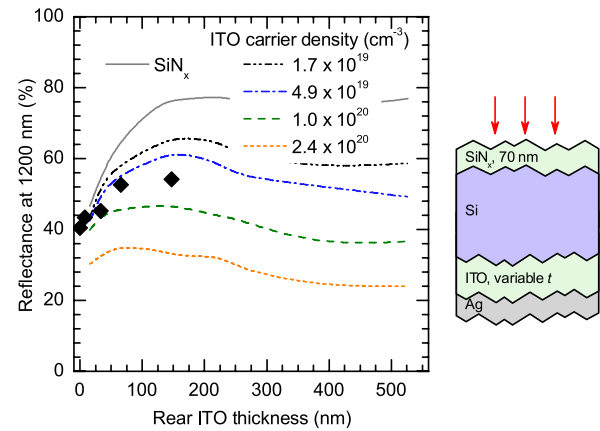

FIG. 14. Simulated total reflectance of 1200 nm light incident on textured wafers with front SiN_x layers and SiN_x/silver or ITO/silver rear stacks. The black diamonds correspond to the measured reflectance of the complete solar cells in Fig. 5, which differ slightly from the simulated structures in that they have transparent ITO in place of the SiN_x front layer. The carrier density of the rear ITO layers in the measured samples varies somewhat, decreasing from approximately $10^{20} \, cm^{-3}$ for the thinnest layer to $10^{19} \, cm^{-3}$ for the thickest. Simulations were performed for ten rear ITO thicknesses, and splines were fit to the results. The random pyramid texture in Fig. 13(a) was used for all simulations.

D. Front vs. rear TCO

Which TCO layer is more important in determining IR current losses in heterojunction cells: the front or the rear? The simulations in Figs. 10 and 11 hint at the answer; we now address the question with experiments. In Fig. 15, the measured reflectance at 1200 nm is plotted for samples for which the front (rear) TCO was replaced with SiN_x, while the carrier density of the rear (front) ITO layer was varied. As 1-*R* at 1200 nm is a metric of parasitic absorption, these experiments allow us to evaluate the relative IR absorption in the front and rear ITO layers independently. The front and rear layer thicknesses for all samples were 69 ± 4 nm and 205 ± 8 nm, similar to the previously identified best thicknesses for each layer. a-Si:H layers were again omitted.
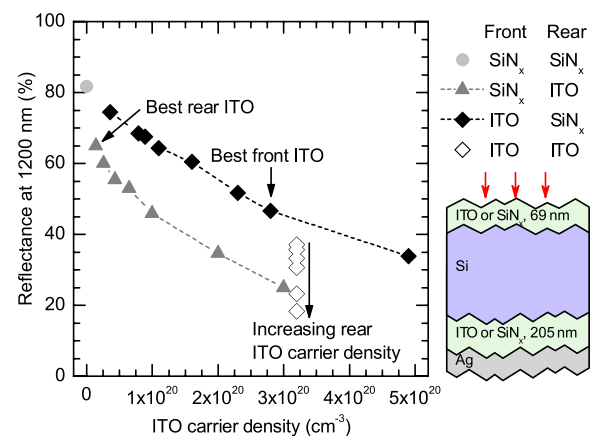

FIG. 15. Reflectance at 1200 nm of textured wafers with SiN_x and ITO layers at the front and rear, and silver reflectors. The front layer thickness was fixed at 69 ± 4 nm and the rear layer at 205 ± 8 nm. The mobility of all ITO films was $30 \pm 10 \, cm^2/Vs$. The x-axis is the carrier density of the ITO layer for samples that have just one (whether it be on the front or rear), and that of the front ITO layer for samples with ITO on both sides (open black diamonds). All SiN_x layers of the same thickness were co-deposited.

A control sample had SiN_x layers on both the front and rear (solid light grey circle). The reflectance of this sample is 82%, and hence 18% of incident light is absorbed parasitically in the silver reflector. If the front SiN_x layer is replaced with ITO (solid black diamonds), the reflectance decreases gradually with increasing ITO doping. These data represent an upper bound for reflectance when front ITO layers of the specified carrier density are employed. That is, replacing the rear SiN_x layer with ITO will only further decrease reflectance (open black diamonds), since the SiN_x layer behaves optically like non-absorbing ITO. The open black diamonds correspond to samples for which the front ITO was fixed at $N = 3.2 \times 10^{20}\,cm^{-3}$ and the rear ITO was varied from $N = 3 \times 10^{20}$–$3 \times 10^{19}\,cm^{-3}$. If, instead, the rear SiN_x layer in the control sample is replaced with ITO and the front remains SiN_x, reflectance falls dramatically with increasing carrier density (solid grey triangles). These data form a reflectance upper bound when rear ITO layers of the specified doping are used, analogous to the front. Provided the carrier densities are known, Fig. 15 can be used to conclude whether IR reflectance—and, by extension, *EQE*—is limited by the front or rear ITO layer in complete solar cells. This is done by locating the point on the black curve corresponding to the front ITO carrier density, and the point on the grey curve corresponding to the rear ITO carrier density. The limiting layer is the layer associated with the lower of the two points. The analysis can be extended to other TCO materials with similar refractive indices by multiplying the x-axis by the ratio of the mobilities, $\mu_{new\,TCO}/\mu_{ITO}$, in accordance with the Drude model of free-carrier absorption. At first glance, it appears that parasitic absorption in the rear ITO layer limits the performance of our standard cells at long wavelengths, since reflectance at 1200 nm is more sensitive to the rear ITO carrier density. Indeed, if $N > 10^{20}\,cm^{-3}$ for the rear ITO, it almost certainly will be responsible for the bulk of the IR parasitic absorption. However, the front ITO layer is restricted to $N \approx 3 \times 10^{20}\,cm^{-3}$ (for $\mu = 30\,cm^2/Vs$ and the optimum finger spacing of 2.2 mm) by the *FF-J$_{sc}$* trade-off, whereas we found that the rear ITO can and should be made as transparent as possible. Thus, as indicated in Fig. 15, for these optimized layers, the front ITO layer is the greater limitation, and materials development efforts should be biased toward its improvement. Figure 15 also explains why 1-*R* and *EQE* changed little in Fig. 7 when the rear ITO carrier density was reduced from 6.5×10^{19} to $2.6 \times 10^{19}\,cm^{-3}$. For these transparent rear layers, the front ITO dominates the loss, and further improving the rear ITO has only a minor effect on cell performance.

We have not yet addressed *why* reflectance at 1200 nm is more sensitive to the rear ITO doping than the front. One possibility is that the somewhat different paths light may take upon arriving from the silicon bulk at the front or rear ITO layers (illustrated in Fig. 9) cause increased absorption in the rear. In particular, light with $\theta < \theta_{c,\,Si/air} = 17°$ propagates through the front ITO only once, and then exits the cell, whereas it passes through the rear ITO twice. Another explanation is the much greater thickness of the rear ITO layer, which increases absorption of both propagating and evanescent waves.
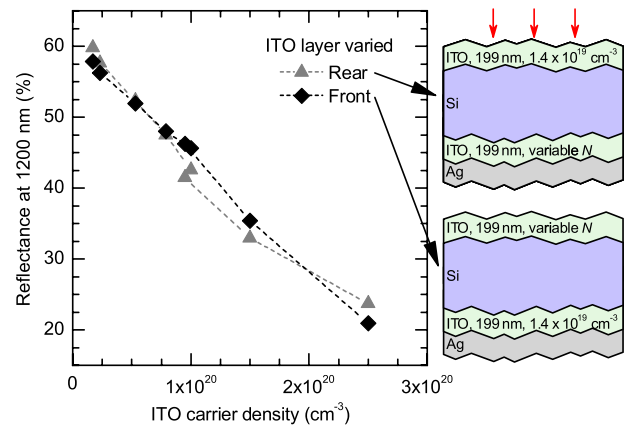

FIG. 16. Reflectance at 1200 nm of textured wafers with ITO layers at the front and rear, and silver reflectors. All layers were 199 ± 12 nm thick with mobilities of 22 ± 11 cm^2/Vs. The x-axis is the carrier density of the ITO layer that was varied (whether it be on the front or rear). The other layers were co-deposited on all samples and were very transparent.

To investigate the latter possibility, we prepared samples similar to those in Fig. 15 but with layers of the same thickness (199 ± 12 nm) deposited on both sides of the wafers. This thickness was chosen because Figs. 13 and 14 indicate that for this thickness, at least at the rear, reflectance is insensitive to small layer thickness variations between samples. Thickness variations would have introduced a much larger error in our measurements if the target thickness was instead, e.g., 50 nm. The SiN_x layers in Fig. 15 were replaced with co-deposited highly transparent ITO layers ($N = 1.4 \times 10^{19}\,cm^{-3}$), although the experiment would have been equally instructive with a SiN_x film on one side of every sample. The carrier density of the other ITO layer was varied, as in Fig. 15. The results are shown in Fig. 16 and reveal that reflectance at 1200 nm has the same dependence on the doping of both ITO layers, provided their thicknesses are equal. We conclude that the difference in pathlength of light with low angles of incidence does not significantly alter the total contributions of the front and rear TCO layers to IR parasitic absorption. Rather, the greater sensitivity of the IR spectral response of an optimized heterojunction solar cell to the rear ITO carrier density is attributable to that layer's greater thickness. This thickness remains optimal nonetheless; Figs. 14 and 15 taken together prescribe a rear TCO layer roughly 150 nm thick, but only if it is very transparent.

IV. CONCLUSION

There is little freedom to adjust the front TCO layer in silicon heterojunction solar cells because it serves simultaneous optical and electrical roles. Increasing its carrier mobility is the only route to improvement. The rear TCO, however, can and should be designed to behave as an optical layer that minimizes absorption of evanescent waves in the metal reflector, in addition to its principal role as an (materials-system-dependant) electrical contact layer. The same is true—save the contact requirement—of the rear dielectric layer in rear-passivated diffused-junction silicon solar cells. In a future contribution, we intend to calculate the reflectance

and J_{sc} losses in such cells with a variety of rear dielectrics and metal reflectors.

We recently reported a 4-cm^2 silicon heterojunction solar cell on a 250-μm-thick wafer that employed TCO layers optimized according to the present study and achieved a certified efficiency of 22.1% with $J_{sc} = 38.9$ mA/cm^2.[1] For this optimized cell, more than 0.5 mA/cm^2 remains to be squeezed out of the IR by further reducing parasitic absorption, e.g., with a locally contacted low-n rear dielectric reflector. For thinner cells, like the latest Sanyo record cell on 98-μm-thick wafers,[49] the potential gains are considerably larger since IR light interacts with the lossy front and rear surfaces many more times per distance traveled through the wafer absorber.

Though we focused on the optical properties of TCO layers here, we noted that optical optimization can progress only if adequate electrical contact is made between the TCO layers and the metal and doped a-Si:H layers between which they are sandwiched. Poor contacts can quickly inflate the series resistance or create reversed diodes that produce S-shaped curves, as we observed when the rear ITO layer was omitted (Fig. 4). A thorough experimental investigation of TCOs as electrical contacts in silicon heterojunctions—with particular attention to a-Si:H Fermi level, TCO work function and carrier density, and metal work function—would thus provide a useful platform on which to build the materials search prescribed by the present optical analysis.

ACKNOWLEDGMENTS

[1]A. Descoeudres, Z. C. Holman, L. Barraud, S. Morel, S. De Wolf, and C. Ballif, IEEE J. Photovoltaics http://dx.doi.org/10.1109/JPHOTOV.2012.2209407 (2012).

[2]M. J. Kerr and A. Cuevas, J. Appl. Phys. **91**, 2473 (2002).

[3]M. A. Green, IEEE Trans. Electron Devices **31**, 671 (1984).

[4]T. Tiedje, E. Yablonovitch, G. D. Cody, and B. G. Brooks, IEEE Trans. Electron Devices **31**, 711 (1984).

[5]Z. C. Holman, A. Descoeudres, L. Barraud, F. Zicarelli, J. P. Seif, S. De Wolf, and C. Ballif, IEEE J. Photovoltaics **2**, 7 (2012).

[6]J. M. Gee, in *Conference Record of the Twentieth IEEE Photovoltaic Specialists Conference*, Las Vegas, NV, 26–30 September 1988, pp. 549–554.

[7]M. Boccard, P. Cuony, C. Battaglia, M. Despeisse, and C. Ballif, Phys. Status Solidi (RRL) **4**, 326 (2010).

[8]E. Yablonovitch, J. Opt. Soc. Am. **72**, 899 (1982).

[9]P. Campbell and M. A. Green, J. Appl. Phys. **62**, 243 (1987).

[10]D. Kray, M. Hermle, and S. W. Glunz, Prog. Photovoltaics Res. Appl. **16**, 1 (2008).

[11]H. W. Deckman, C. R. Wronski, H. Witzke, and E. Yablonovitch, Appl. Phys. Lett. **42**, 968 (1983).

[12]S. Pillai, K. R. Catchpole, T. Trupke, and M. A. Green, J. Appl. Phys. **101**, 093105 (2007).

[13]H. Stiebig, N. Senoussaoui, C. Zahren, C. Haase, and J. Muller, Prog. Photovoltaics Res. Appl. **14**, 13 (2006).

[14]C. Battaglia, C. M. Hsu, K. Soderstrom, J. Escarre, F. J. Haug, M. Charriere, M. Boccard, M. Despeisse, D. T. L. Alexander, M. Cantoni, Y. Cui, and C. Ballif, ACS Nano **6**, 2790 (2012).

[15]M. D. Kelzenberg, S. W. Boettcher, J. A. Petykiewicz, D. B. Turner-Evans, M. C. Putnam, E. L. Warren, J. M. Spurgeon, R. M. Briggs, N. S. Lewis, and H. A. Atwater, Nature Mater. **9**, 239 (2010).

[16]E. Moulin, U. W. Paetzold, J. Kirchhoff, A. Bauer, and R. Carius, Phys. Status Solidi (RRL) **6**, 65 (2012).

[17]A. Descoeudres, L. Barraud, S. De Wolf, B. Strahm, D. Lachenal, C. Guerin, Z.C. Holman, F. Zicarelli, B. Demaurex, J. Seif, J. Holovsky, and C. Ballif, Appl. Phys. Lett. **99**, 123506 (2011).

[18]M. Buchanan, J. B. Webb, and D. F. Williams, Appl. Phys. Lett. **37**, 213 (1980).

[19]C. Battaglia, L. Erni, M. Boccard, L. Barraud, J. Escarre, K. Soderstrom, G. Bugnon, A. Billet, L. Ding, M. Despeisse, F. J. Haug, S. De Wolf, and C. Ballif, J. Appl. Phys. **109**, 114501 (2011).

[20]J. N. Hilfiker N. Singh, T. Tiwald, D. Convey, S. M. Smith, J. H. Baker, and H. G. Tompkins, Thin Solid Films **516**, 7979 (2008).

[21]F. Abeles, J. Phys. Radium **11**, 307 (1950).

[22]K. Ohta and H. Ishida, Appl. Opt. **29**, 1952 (1990).

[23]G. E. Jellison, Jr., Opt. Mater. **1**, 41 (1992).

[24]E.D. Palik, *Handbook of Optical Constants of Solids* (Academic, San Diego, 1997).

[25]B. Lipovsek, J. Krc, and M. Topic, Inform. Midem **41**, 264 (2011).

[26]P.Y. Yu and M. Cardona, *Fundamentals of Semiconductors: Physics and Materials Properties*, 4 ed. (Springer, Heidelberg, 2010).

[27]A. Favier, D. Munoz, S. M. de Nicolas, and P. J. Ribeyron, Sol. Energy Mater. Sol. Cells **95**, 1057 (2011).

[28]G. Choong, P. Bole, L. Barraud, F. Zicarelli, A. Descoeudres, S. De Wolf, and C. Ballif, in *Proceedings of the European Photovoltaic Solar Energy Conference and Exhibition*, Valencia, Spain, 6–10 September 2010.

[29]M. Bivour, C. Reichel, M. Hermle, and S. W. Glunz, Sol. Energy Mater. Sol. Cells **106**, 11–16 (2012).

[30]L. Zhao, C. L. Zhou, H. L. Li, H. W. Diao, and W. J. Wang, Phys. Status Solidi A **205**, 1215 (2008).

[31]F. S. Sinencio and R. Williams, J. Appl. Phys. **54**, 2757 (1983).

[32]H. Schade and Z. E. Smith, J. Appl. Phys. **59**, 1682 (1986).

[33]L. J. Brillson and Y. Lu, J. Appl. Phys. **109**, 121301 (2011).

[34]L. Zhao, C. L. Zhou, H. L. Li, H. W. Diao, and W. J. Wang, Sol. Energy Mater. Sol. Cells **92**, 673 (2008).

[35]P. Cuony, D. T. L. Alexander, I. Perez-Wurfl, M. Despeisse, G. Bugnon, M. Boccard, T. Soderstrom, A. Hessler-Wyser, C. Hebert, and C. Ballif, Adv. Mater. **24**, 1182 (2012).

[36]C. Simeon, B.-Finch, and K. R. McIntosh, Prog. Photovoltaics Res. Appl. **19**, 406 (2011).

[37]M. Balestrieri, D. Pysch, J. P. Becker, M. Hermle, W. Warta, and S. W. Glunz, Sol. Energy Mater. Sol. Cells **95**, 2390 (2011).

[38]N. J. Harrick and F. K. Dupre, Appl. Opt. **5**, 1739 (1966).

[39]N. J. Harrick, J. Opt. Soc. Am. **55**, 851 (1965).

[40]N. J. Harrick and A. I. Carlson, Appl. Opt. **10**, 19 (1971).

[41]Y. Ishino and H. Ishida, Appl. Spectrosc. **42**, 1296 (1988).

[42]A. Hatta, T. Ohshima, and W. Suetaka, Appl. Phys. A **29**, 71 (1982).

[43]A. Otto, Z. Phys. **216**, 398 (1968).

[44]J. Springer, A. Poruba, L. Mullerova, M. Vanecek, O. Kluth, and B. Rech, J. Appl. Phys. **95**, 1427 (2004).

[45]F. J. Haug, T. Soderstrom, O. Cubero, V. Terrazzoni-Daudrix, and C. Ballif, J. Appl. Phys. **104**, 064509 (2008).

[46]N. N. Lal, H. Zhou, M. Hawkeye, J. K. Sinha, P. N. Bartlett, G. A. J. Amaratunga, and J. J. Baumberg, Phys. Rev. B **85**, 245318 (2012).

[47]H. W. Deckman, C. B. Roxlo, and E. Yablonovitch, Opt. Lett. **8**, 491 (1983).

[48]P. Campbell, S. R. Wenham, and M. A. Green, Sol. Energy Mater. Sol. Cells **31**, 133 (1993).

[49]T. Kinoshita, D. Fujishima, A. Yano, A. Ogane, S. Tohoda, K. Matsuyama, Y. Nakamura, N. Tokuoka, H. Kanno, H. Sakata, M. Taguchi, and E. Maruyama, in *Proceedings of the European Photovoltaic Solar Energy Conference and Exhibition*, Hamburg, Germany, 5–9 September 2011.